Effects of cirrus heterogeneity on lidar CALIOP/CALIPSO data

Alaa Alkasem, Frédéric Szczap, Céline Cornet, Valery Shcherbakov, Yahya Gour, Olivier Jourdan, Laurent Labonnote, Guillaume Mioche

Effects of cirrus heterogeneity on lidar CALIOP/CALIPSO data

A. Alkasem , F. Szczap , C. Cornet , V. Shcherbakov , Y. Gour , O. Jourdan , L.C. Labonnote , G. Mioche

PII: S0022-4073(17)30130-9
DOI: 10.1016/j.jqsrt.2017.07.005
Reference: JQSRT 5772

To appear in: *Journal of Quantitative Spectroscopy & Radiative Transfer*

Received date: 16 February 2017
Revised date: 6 July 2017
Accepted date: 7 July 2017

Please cite this article as: A. Alkasem , F. Szczap , C. Cornet , V. Shcherbakov , Y. Gour , O. Jourdan , L.C. Labonnote , G. Mioche , Effects of cirrus heterogeneity on lidar CALIOP/CALIPSO data, *Journal of Quantitative Spectroscopy & Radiative Transfer* (2017), doi: 10.1016/j.jqsrt.2017.07.005

Highlights

- Heterogeneous cirrus clouds are generated.
- Lidar signals are simulated using a Monte-Carlo code.
- Effects on CALIOP lidar measured data are evaluated.
- Importance of horizontal photon transport is underscored.

Effects of cirrus heterogeneity on lidar CALIOP/CALIPSO data

A. Alkasem[a], F. Szczap[a,*], C. Cornet[b], V. Shcherbakov[a,c], Y. Gour[a], O. Jourdan[a], L.C.-Labonnote[b] and G. Mioche[a]

[a]Université Clermont Auvergne, CNRS, UMR 6016, Laboratoire de Météorologie Physique, F-63000 Clermont-Ferrand, France

[b]Université Lille, CNRS, UMR 8518 - LOA - Laboratoire d'Optique Atmosphérique, F-59000 Lille, France

[c]Université Clermont Auvergne, Institut Universitaire de Technologie d'Allier, Montluçon, France

* Corresponding author. Tel.: +33 4 73 40 73 57.

E-mail address: szczap@opgc.univ-bpclermont.fr (F. Szczap).

Abstract

The goal of this work is to evaluate the effects of cirrus heterogeneity on characteristics that are directly measured by the CALIOP/CALIPSO lidar, i.e. attenuated backscatter coefficient and depolarization ratio. This assessment was done using the 3D Monte Carlo simulator of Polarized Lidar signals (3DMcPOLID) together with the high-resolution 3D cloud fields-generator 3DCLOUD_V2. The evaluation is based on random sampling and on comparison between mean profiles of 3D clouds and of plane-parallel equivalent 1D clouds.

Mean profiles of the apparent attenuated backscatter as well as of the integrated apparent backscatter are statistically equal when a cirrus cloud field is probed with the 325 m resolution. To the contrary, the difference between profiles is statistically significant in the case of the 1 km resolution. Profiles of the volume depolarization ratio are statistically different for both cases of the horizontal resolution. The total bias of CALIOP/CALIPSO lidar data is mainly due to the plane parallel bias and multiple scattering, i.e., horizontal photon transport.

Keywords

Radiative transfer, heterogeneous clouds, cirrus, lidar, backscatter, polarization

1. Introduction

Clouds have a significant effect on the Earth radiation budget. They reflect the solar radiation and reduce the warming of the Earth (albedo effect). They also contribute to the greenhouse effect by trapping the thermal radiation emitted from the Earth's surface, reducing the radiative cooling of the Earth (see, e.g., [1,2] and references therein).

Nowadays, remote sensing, i.e., spaceborne passive and active instruments, is the principal source of information on global Earth clouds and precipitations characteristics. Passive sensors have a broad area of coverage. Active sensors, as radars and lidars, provide range-resolved profile measurements. *"Major challenges engaged in the characterization of clouds by remote sensing methods are confronted. The problems come, on the one hand, from the spatial heterogeneity of real clouds and, on the other hand, from the dominance of multiple scattering in the radiation transport"* [3]. Scientific literature addressing effects of 3D radiative transfer within cloud fields is large and has multiple decades of history (see, e.g., [3] and references therein). It was proven that cloud heterogeneity is a major factor that strongly affects the passive remote sensing of some cloud properties (see, e.g., [4].

Concerning active sensors, it has long been known that incomplete beam filling affects data of radar sounding (see, e.g., [5, 6]). The field of view (FOV) of radars, as a rule, is quite large and hence signals depend on a spatially heterogeneous but unresolved rain field within the FOV. That problem, as applied to spaceborne radars, is referred to as non-uniform beam filling (NUBF). Biases in radar-retrieved rain rate due to NUBF have been addressed by a number of authors (see, e.g., [7], and references therein).

The Cloud-Aerosol Lidar with Orthogonal Polarization (CALIOP) onboard the Cloud-Aerosol Lidar and Infrared Pathfinder Satellite Observations (CALIPSO) satellite part of the so-called 'A-train' constellation was developed to provide global profiling measurements of cloud and aerosol and properties in order to complement current measurements and improve our understanding of weather and climate [8,9].

Lidar-data interpretation is usually based on the single-scattering lidar-equation that excludes the effects of multiple scattering (MS). In the case of lidar cloud sounding, such an assumption can lead to huge errors. Numerous scientific works addressed that problem.

Results of the MUSCLE (Multiple Scattering Lidar Experiment) working group are especially interesting (see [10] and references therein). In his review, Bissonnette [11] concludes that "*multiple scattering in lidar manifests itself as greater signal strength and alteration of polarization. These effects depend on the measurement geometry (in particular the distance to the scattering medium and the physical penetration depth), on the system parameter (most importantly the receiver field of view) and on the medium properties (i.e., the extinction coefficient, the angular scattering function, and the optical depth)*".

Owing to the highly narrow FOV of lidars, there is no need to account for incomplete beam filling for ground-based or airborne measurements of the atmosphere. The cross section of the laser beam is always lower than the characteristic size (or correlation length) of the heterogeneity of aerosol/cloud fields. Thus, the model of plane parallel clouds is universally accepted in lidar signal calculations (direct problem) and in cloud-property retrievals (inverse problem). However, spaceborne lidars such as CALIOP/CALIPSO have a quite large laser footprint, so that a cloud field can be horizontally heterogeneous within the footprint. This raises the well-known problem of non-uniform beam filling (NUBF), but applied to the lidar remote sensing.

Clouds show complex tridimensional (3D) variability in their horizontal and vertical geometrical, optical and microphysical properties at different averaging scales. For example, the power spectra of the logarithm of their optical and microphysical properties (optical depth, liquid water content or liquid water path for low clouds and ice water content for high clouds) typically exhibits a spectral slope of around $-5/3$ [12–20] from small scale (a few meters) to the "integral scale" or the outer scale (a few tens of kilometers to one-hundred kilometers), where the spectrum becomes flat (i.e. decorrelation occurs). At the same time, very few scientific contributions address the effect of cloud heterogeneity on lidar measurement. Miller and Stephens [21] carried out a brief exploration of lidar pulse extension behavior in non-uniform horizontal/vertical media with 3D Monte Carlo lidar model, and concluded that detailed cloud geometries effects were not negligible. Albers et al. [22] calculated backscatter intensity from measured in-situ data, showing that cloud inhomogeneities cannot be neglected in the interpretation of remote sensing data.

The effects of the NUBF of spaceborne lidars are twofold. *(i)* Characteristics that are directly measured by lidar, i.e., the attenuated backscatter coefficient and the depolarization ratio, can be affected by heterogeneity and lead to biased cloud statistics derived from measurements. Heterogeneity effects have thus to be quantified with respect to direct radiative transfer

calculations, i.e., simulation of lidar/radar observations. *(ii)* Retrievals from lidar observations of cloud parameters, as optical thickness, can be affected as well. Retrieval errors need detailed investigations, which should be done on the base of direct simulations.

The objective of this work is to evaluate how 3D cirrus heterogeneity affects CALIOP/CALIPSO lidar data under conditions of multiple scattering. It should be stressed that we are dealing with only one of numerous error sources related to the direct problem, i.e., to forward-modelled lidar data. The evaluations were performed using an approach well-known in the radiative-transfer community (see, e.g., [3] and references therein). The approach consists of comparing mean radiative properties of the 3D clouds and those of the homogenous and plane-parallel equivalent clouds that have the same optical properties as the 3D clouds on the average. We developed two tools for this purpose. The first one is the 3D polarized lidar simulator (3DMcPOLID) which is based on the 3DMCPOL model [23], employed to simulate 3D radiance on the top of the atmosphere measured by passive sensors. The second tool is a high-resolution synthetic 3D cloud fields-generator (3DCLOUD_V2). It is an enhanced version of the 3DCLOUD model [20], where a wavelet framework is used instead of Fourier framework.

The organization of this paper is as follows. In section 2, we detail the methodology used to quantify 3D cloud inhomogeneity effects on CALIOP/CALIPSO measurements. The cirrus cloud fields generated by 3DCLOUD_V2 are then presented. In section 3, quantitative effect of cloud inhomogeneities on the apparent backscatter, the integrated apparent backscatter and the volume depolarization ratio as measured by CALIOP/CALIPSO are presented. Conclusions and discussions are presented in section 4. The 3DMcPOLID algorithm is presented in appendix A and its performance is outlined.

2. Methodology

2.1. Synthetic inhomogeneous cirrus cloud fields generated by 3DCLOUD_v2

3DCLOUD [20] is a fast and flexible algorithm designed to generate realistic 3D cloud fields for stratocumulus, cumulus and cirrus. Cloud fields can be simulated in terms of extinction coefficient (ε), local optical depth (τ) or liquid/ice water path (LWP/IWP). The generated

fields have statistical properties that are in agreement with observations in real clouds. It is assumed that the optical depth follows a gamma distribution. The parameters used for radiative transfer calculations are the mean optical depth $\overline{\tau}$, the inhomogeneity parameter ρ (standard deviation of τ normalized by the mean of τ), the cloud coverage C, and the Fourier spectral slope β (which is close to −5/3 between the smallest scale of the simulation to the outer L_{out} where the spectrum becomes flat).

In the first step, 3DCLOUD solves drastically simplified basic atmospheric equations and assimilates the user's prescribed large scale meteorological profiles (humidity, pressure, temperature and wind speed), in order to simulate 3D structures of liquid water content (LWC) or ice water content (IWC). In the second step, the iterative Fourier filtering method is used to constrain the intensity of $\overline{\tau}$, ρ, β and L_{out}. It should be underscored that for anisotropic cloud fields such as cirrus uncinus with pronounced preferred direction of fall-streaks, the used Fourier filtering method gives sometimes unusual cirrus structures with sharp variations in the final 3D extinction field. Such structures have a spectral slope $\beta \geq 0$ at high frequencies in Fourier energy spectrum (see Fig. 2c) which contradicts experimental observations. Therefore, we developed 3DCLOUD_V2 code, an enhanced version of the 3DCLOUD model, where the wavelet framework is used instead of the Fourier framework in the second step. It is well known that wavelets are localized in both space and frequency whereas the standard Fourier transform is localized only in frequency. Thus, we expect that the new iterative wavelet method operating during the second step of 3DCLOUD_v2 algorithm will allow a better control of the spectral slope value without affecting the spatial structure of the cloud simulated during the second step of 3DCLOUD model.

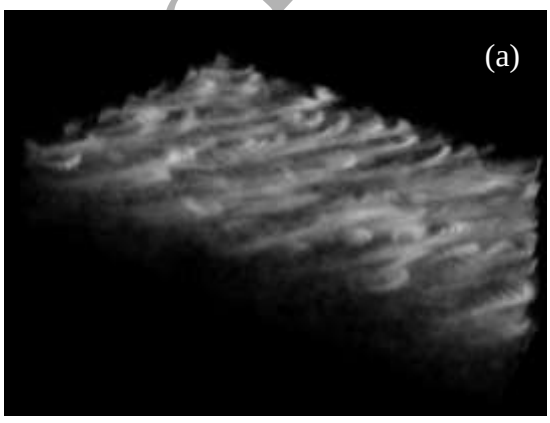

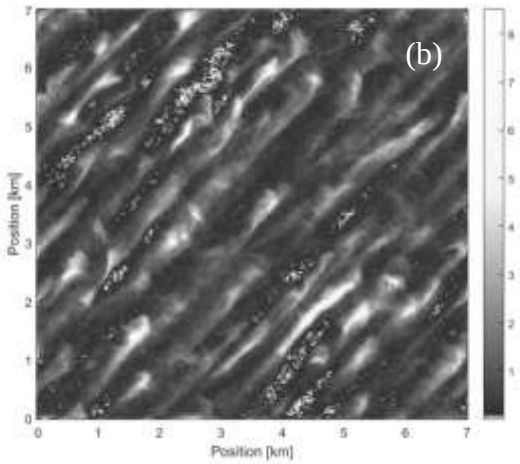

Figure 1 : (a) Volume rendering and (b) optical thickness of cirrus used in this study.

We present some textural and statistical properties of the cirrus generated by 3DCLOUD_v2 and used in this study. Large scale meteorological profiles assimilated by 3DCLOUD_v2 during the first step (wind speed, humidity, temperature) are similar to those presented in [20].

Snapshots of the cirrus structure are display on Fig. 1. The optical thickness field generated by the wavelet framework at the end of the second step of 3DCLOUD_V2 is show on Fig. 1b. The mean optical depth is $\bar{\tau} = 0.98$; and the inhomogeneity parameter, i.e., the ratio of the standard deviation of the optical depth to the mean optical depth is $\rho_\tau = 0.91$. The horizontal extension is 7 km, the vertical resolution is 60 m and the horizontal resolution is 25 m both in x and y directions. The specific values of $\bar{\tau}$ and ρ_τ were chosen on the base of in situ observations performed by Gayet et al. [24] in midlatitude cirrus clouds of the Southern and the Northern hemispheres. They are in good agreement with the values used in the works by Fu et al. [25] and Carlin et al. [26]. If the pixel size is of 450 m, the inhomogeneity parameter of our cirrus field $\rho_\tau = 0.50$ is in agreement with Table 1 of the review by Shonk et al. [27].

In order to underscore the advantage of the wavelet framework, Fig. 2 shows statistical properties of cirrus fields generated by 3DCLOUD and 3DCLOUD_V2 codes. Fig. 2a displays an histogram of the 3D extinction coefficients. Vertical profiles of horizontally averaged ice water content (IWC) and extinction coefficient are represented in Fig. 2b. It is seen that the base and the top altitudes of the cirrus field are around 9.2 km and 10.8 km, respectively. Fig. 2c shows mean 1D power spectra of the IWC generated by 3DCLOUD at the step 1 and of the extinction generated at the step 2 by 3DCLOUD and 3DCLOUD_V2, respectively. The IWC field is very smooth. Such smoothness leads to the spectral slope that is close to -5.5 for the scale smaller than 1 km (Fig. 2c). Optical depth field generated by 3DCLOUD and 3DCLOUD_V2 are rougher. Both 3D extinction fields have a spectral slope close to -1.6 (Fig. 2c). The 3D extinction histograms (Fig. 2a) and the averaged profiles (Fig. 2b) are very close to each other; and we can note their gamma-like distribution. However, the extinction field generated by 3DCLOUD has some sharp discontinuities whereas it is not the case in the field generated by 3DCLOUD_V2. This drawback leads to 1D flat spectral slope of 3DCLOUD extinction at the highest wavenumbers. The wavelet framework seems to be a good alternative. Contrary to Fourier framework, the extinction field does not show a 1D spectral slope close to zero at the highest wavenumbers.

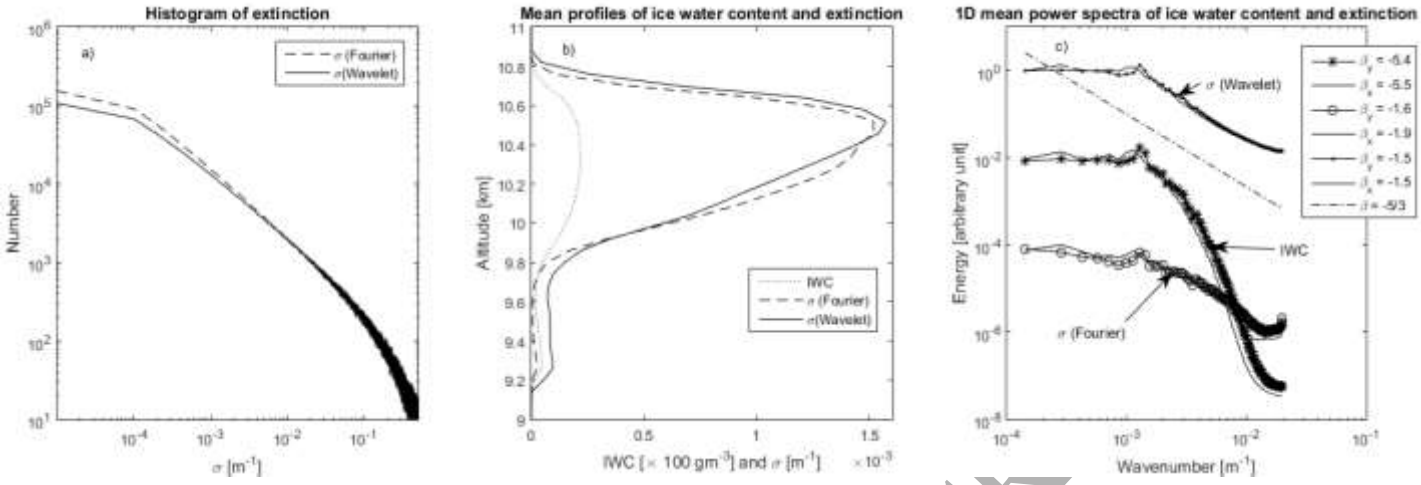

Figure 2: (a) Histogram of 3D extinction and (b) mean profiles of ice water content (dotted line) and 3D extinction generated by 3DCLOUD (dashed line) and 3DCLOUD_V2 (full line). (c) Mean 1D power spectra of IWC (star), 3DCLOUD (circle), 3DCLOUD_V2 (point) following x direction (full lines for y direction) and of theoretical signal with 1D spectral slope of $-5/3$. Numerical values of 1D spectral value, estimated between from 10^{-3} m^{-1} wavenumber to the Nyquist wavenumber, following x and y directions, are given. Power spectra are vertically shifted for reasons of clarity.

2.2. Methodology applied to compare 1D and 3D lidar signals

CALIOP products contain profiles of attenuated backscatter $\beta(h)$ that can be written in the single-scattering approximation as [28]:

$$\beta(h) = \left[\beta_p(h) + \beta_m(h)\right] \cdot T^2(h), \quad (1)$$

where $\beta_p(h)$ and $\beta_m(h)$ represent the backscatter contributions from particles and from the atmospheric molecules, and $T^2(h)$ represents the two-way transmittance between the satellite and the altitude level h. The integrated attenuated backscatter is expressed as:

$$I(h) = \int_h^{h_0} \beta(z)\, dz. \quad (2)$$

where h_0 is the altitude of the cloud top.

CALIPSO orbits at an altitude of 705 km. CALIOP's transmitter has a beam divergence of 0.11 mrad; and the receiver has a field of view (FOV) of 0.13 mrad [28–29]. Such a large distance from the clouds to the receiver leads to two important consequences. The first

consequence is linked to the so-called configuration angle θ_c, which is proportional to the FOV and to the distance to cloud (see Eq. (5) in [30]). The single-scattering lidar equation is valid if $\theta_c \ll \theta_d$, where θ_d is the diffraction angle of ice crystals [30]. In the case of the CALIOP configuration $\theta_c \approx \theta_d$. In other words, a significant fraction of the scattering energy is included in a small angle forward lobe and may stay in the lidar receiver FOV [31]. That fact is confirmed by our simulations for homogeneous cirrus (not shown here). It turns out that the ratio of multiple-scattering contribution to single-scattering contribution for CALIOP lidar return can reach 30 % even for the low optical depth of 0.15. Thus, CALIOP signals from cirrus are affected by multiple scattering. In order to underscore that fact we use in this work the term "apparent attenuated backscatter" instead of the "attenuated backscatter" (see, e.g., [32–33]). Consequently, we investigate effects of cirrus heterogeneity on CALIOP lidar data in multiple-scattering conditions.

The second consequence is the fact that the diameter of the CALIOP laser footprint is about 70 meters [34]. It is sufficiently large so that lidar signals can be affected by heterogeneity of cirrus clouds, especially when the footprint overlaps an edge of a cloud. From the point of view of the atmospheric optics, the effect has much in common with the problem of partly cloudy pixels in Moderate Resolution Imaging Spectroradiometer (MODIS) cloud property retrievals (see, e.g., [35] and references therein). Thus, the effect has to be thoroughly evaluated.

The evaluation of the heterogeneity effects has to be based on a radiative-transfer community approach. That is, we have to compare two sets of optical characteristics (in this case, lidar data). One set is representative of 3D cloud fields and another set corresponds to the horizontally homogenous and plane-parallel equivalent clouds. In this work the plane-parallel model allows vertical layering. Therefore the equivalent 1D cloud has the same optical characteristics as the corresponding horizontally averaged 2D-cloud field.

However, the evaluation of the heterogeneity effects also needs to be adapted to the peculiarities of the CALIOP data acquisition. Specifically, CALIOP samples a cloud field along the track with the fundamental sampling resolution of 30 m vertically and 333 m horizontally [28]. Cloud characteristics are available at three spatial resolutions (the 333-m, the 1-km and 5-km layer-products) over a vertical range extending from ~20.2 km above mean sea level down to -0.5 km below sea level. In this work, we report only results for 325-m (not 333 due to our numerical simulation horizontal resolution of 25 m both in *x* and *y* directions) and 1-km horizontal resolutions.

Simulation of along-track sampling is time-consuming because it requires generation of a large set of high-resolution 3D cloud fields, which are similar in terms of statistical properties of optical and physical characteristics. At the same time, the along-track sampling exploits only a small portion of each generated field. Thus, we preferred random sampling applied to one generated field (see Section 2.1). The random sampling provides satisfactory results when the given high-resolution 3D cloud field is large enough.

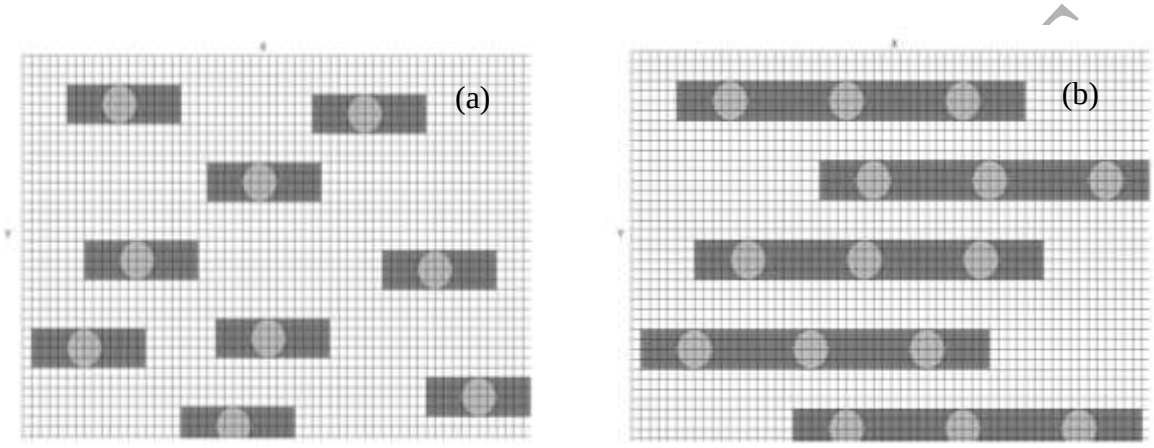

Figure 3. Schematic representations of the random sampling for (a) 325 m horizontal resolution and for (b) 1 km horizontal resolution.

Figure 3a) shows a schematic sketch of the random sampling for the 325 m horizontal resolution. It represents a part of the cloud field as viewed from the top with a resolution of 25m. Observations from the 3D sample are indicated by the dark-gray circles. Every circle is a schematic representation of a receiver footprint. The receiver has a FOV angle of 0.13 mrad and it covers several pixels. The cloud field is horizontally heterogeneous within the footprint, that is, the IWC and the extinction coefficient depend not only on the altitude, but on the x and y coordinates as well. Every photon scattered in the receiver direction within the FOV contributes to the output signal. Due to multiple scattering, a lidar signal is formed by photons travelled within the FOV and coming from neighboring pixels. The 3D lidar data are simulated for each footprint with the 3DMcPOLID code (see Appendix A). Observations from the 1D sample are shown by the dark-gray rectangles. Every rectangle represents the averaging area of the 325 m horizontal resolution in agreement with the assumption made for CALIOP measurements. It includes the corresponding laser footprint. The cloud optical parameters were averaged over the rectangle at every altitude level. The obtained profiles of the averaged values were used to compute the 1D lidar data with the same 3DMcPOLID code, i.e., the data that correspond to the case of a plane-parallel cloud field.

For the 1 km horizontal resolution, the random sampling was performed in the same way (see Fig. 3b). The difference is that every averaging area was a rectangle of 1 km long, and it includes the average of three separate 3D calculations for each CALIPSO footprint in the 1 km boxes.

Two complementary approaches were employed to evaluate the radiative effects of cirrus heterogeneity. The first approach is based on the analysis of relative or absolute errors. Let $P(h)$ be a vertical profile of a particular parameter. The absolute error/bias $\Delta P(h)$ is computed as

$$\Delta P(h) = \langle P(h) \rangle_{1D} - \langle P(h) \rangle_{3D}, \tag{3}$$

where $\langle \cdots \rangle_{1D}$ and $\langle \cdots \rangle_{3D}$ denote averaging over 1D and 3D samples, respectively. The relative error/bias (in percentage) $\delta P(h)$ is computed as

$$\delta P(h) = 100 \cdot \frac{\Delta P(h)}{\langle P(h) \rangle_{3D}} = 100 \cdot \frac{\langle P(h) \rangle_{1D} - \langle P(h) \rangle_{3D}}{\langle P(h) \rangle_{3D}}. \tag{4}$$

On the one hand, the analysis of relative/absolute errors is commonly accepted; on the other hand, it suffers from the following shortcoming. There is no possibility to conclude whether the difference between $\langle P(h) \rangle_{1D}$ and $\langle P(h) \rangle_{3D}$ is statistically significant when a specific value of $\Delta P(h)$ or $\delta P(h)$ is obtained. Thus, we also employed the second approach, namely, *t*-tests that provide a mechanism for making quantitative decisions. The basic terminology, methods and equations of descriptive statistics used in this work can be found, for example, in the book by Sheskin [36]. The equality of means is employed as the null hypothesis in this work, that is,

$$H_0: \langle P(h) \rangle_{1D} = \langle P(h) \rangle_{3D}. \tag{5}$$

It should be emphasized that the computed *t*-values are somewhat normalized to the estimated variances and covariance (see Eq. (6) below) and thus they do not depend on the magnitude of the parameter $P(h)$.

Despite the fact that Monte-Carlo simulations are time consuming, the size of the samples is chosen to be large, i.e., of $N = 200$ observations. That provides the possibility to ensure the quality of our hypothesis tests. When we deal with lidar data, e.g., apparent attenuated backscatter, the population standard deviation is unknown. Thus, our evaluations are based on *t*-tests, i.e., the single-sample *t*-test or the *t*-test for two dependent samples (see [36] Ch. 2 and Ch. 17). We employed the tabled critical *t*-value of $t_{.05} = 1.96$ that corresponds to the significance level of 0.05 for two-tailed and of 0.025 for one-tailed hypothesis testing.

It follows from the specification above that our 3D and 1D samples are dependent (paired samples A and B). In other words, the samples are related to each other and the covariance (correlation) has to be taken into account when *t*-value is computed ([36], Ch. 17):

$$t = \frac{\langle A\rangle - \langle B\rangle}{\sqrt{[S_A^2 + S_B^2 - 2\mathrm{cov}(A,B)]/N}}, \quad (6)$$

where $\langle \dots \rangle$, $S_{\dots}^2$, and $\mathrm{cov}(\dots)$ denote the estimated mean, variance, and covariance values, respectively.

In addition to standard assumptions necessary for random sampling, the key feature required of our evaluations was the following. The mean profile of the extinction coefficient of a sample, that is, $\langle \varepsilon(h)\rangle_{3D}$ for the 3D sample or $\langle \varepsilon(h)\rangle_{1D}$ for the 1D sample (where h stands for the altitude value) has to be statistically equal to the mean profile $\langle \varepsilon(h)\rangle_{Tot}$ of the cloud field as a whole (see Fig. 2b), i.e., of the population. This means that the null hypothesis of the single-sample *t*-test cannot be rejected. In other words, the computed *t*-value $|t| < 1.96$ for all altitude levels h of the cloud field. Moreover, the mean profiles $\langle \varepsilon(h)\rangle_{3D}$ and $\langle \varepsilon(h)\rangle_{1D}$ of the extinction coefficient of the 3D- and 1D- samples have to be statistically equal. This means that the null hypothesis of the *t*-test for two dependent samples cannot be rejected ($|t| < 1.96$). The profiles $\langle \varepsilon(h)\rangle_{3D}$ and $\langle \varepsilon(h)\rangle_{1D}$ are shown in Fig. 4a.

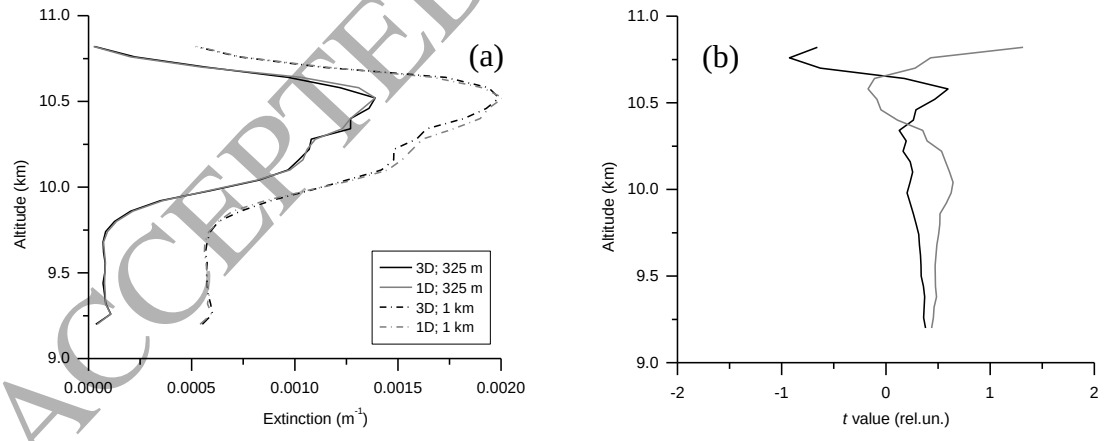

Figure 4. (a) Mean profiles of the extinction coefficient. The black and gray lines correspond to $\langle \varepsilon(h)\rangle_{3D}$ and $\langle \varepsilon(h)\rangle_{1D}$ profiles, respectively. The solid and dash-dot lines correspond to the 325-m and 1-km horizontal resolutions, respectively. The dash-dot lines are shifted by 0.0005 m^{-1}. (b) Profiles of the *t*-value for the optical depth. The black and gray lines correspond to the 325-m and 1-km horizontal resolutions, respectively.

A profile of the cloud optical depth $\tau(h)$ can be readily calculated when the profile of the extinction coefficient $\varepsilon(h)$ is known:

$$\tau(h) = \int_h^{h_0} \varepsilon(z)\, dz, \tag{7}$$

where h_0 is the altitude of the cloud top. The direct consequence of the statistical equivalence of the extinction profiles coefficient $\langle\varepsilon(h)\rangle_{1D}$ and $\langle\varepsilon(h)\rangle_{3D}$ is the fact that the mean profiles of the cloud optical depth $\langle\tau(h)\rangle_{1D}$ and $\langle\tau(h)\rangle_{3D}$ of the 1D and 3D samples are statistically equal (*i*) to one another and (*ii*) to the mean profile $\langle\tau(h)\rangle_{Tot}$ of the cloud field as a whole. That property is confirmed by Fig. 4(b) where the computed *t*-values of the *t*-test for two dependent samples are shown.

In this work, CALIOP/CALIPSO lidar data were simulated with 3DMcPOLID software (see Appendix below) for both 3D and 1D cases. It is assumed that the scattering matrix of cirrus particles was the same for the whole cloud field. The matrix was computed for a gamma size-distribution of ice crystals with an effective diameter of 50 μm. The refractive index value was $m = 1.3117 + i \cdot 2.6139 \cdot 10^{-9}$ at the wavelength 532 nm; the surface of particles was supposed to be deeply rough [37]. Optical characteristics were computed using the improved geometric optics method (IGOM) [37]. The asymmetry parameter is $g = 0.78$, which is in agreement with experimental data for cirrus clouds [24, 38].

In Section 3, we discuss our results in view of the scientific literature published by the 3D radiative transfer community. With this in mind, we will use the terms "plane-parallel (PP) bias" and "independent column approximation (ICA) bias" according to the work of Davis and Polonsky [39] with the only difference in the sign. We define the bias as the estimated value minus the true value and not the reverse. More specifically, let us consider the *i*-th observation $P(h)_{i,3D}$ of the parameter $P(h)$ from the 3D sample and the corresponding observation $P(h)_{i,1D}$ from the 1D sample. Note that there is no averaging over 1D and 3D samples here. Equations (8) and (9) define the PP and ICA biases, respectively,

$$\Delta P(h)_{i,PP} = P(h)_{i,1D} - \langle P(h)\rangle_{i,pixels}, \tag{8}$$

$$\Delta P(h)_{i,ICA} = \langle P(h)\rangle_{i,pixels} - P(h)_{i,3D}, \tag{9}$$

where $\langle\cdots\rangle_{pixels}$ is averaging over the corresponding pixels, that is, $\langle P(h)\rangle_{i,pixels}$ is the profile computed following the independent column approximation for the *i*-th observation. It is evident that the absolute bias of the *i*-th observation is:

$$\Delta P(h)_i = \Delta P(h)_{i,PP} + \Delta P(h)_{i,ICA} = P(h)_{i,1D} - P(h)_{i,3D}. \quad (10)$$

The absolute bias $\Delta P(h)$ of Eq. (3) can be computed by averaging $\Delta P(h)_i$ over the samples.

3. Results

Figure 5 shows a typical example of our Monte-Carlo simulations results. It refers to one of 200 observations that represent our random sampling. On one hand, there are some similarities between the 3D and 1D profiles of the apparent attenuated backscatter. It is reasonable to expect the resemblance because the profiles were obtained for the same regions of the cloud field (see Fig. 3). On the other hand, large relative differences between the 3D and 1D simulations are observed. In such conditions, it makes no sense to compare 3D and 1D lidar data for every observation, instead here we will focus on analyzing the differences in suitably averaged mean profiles.

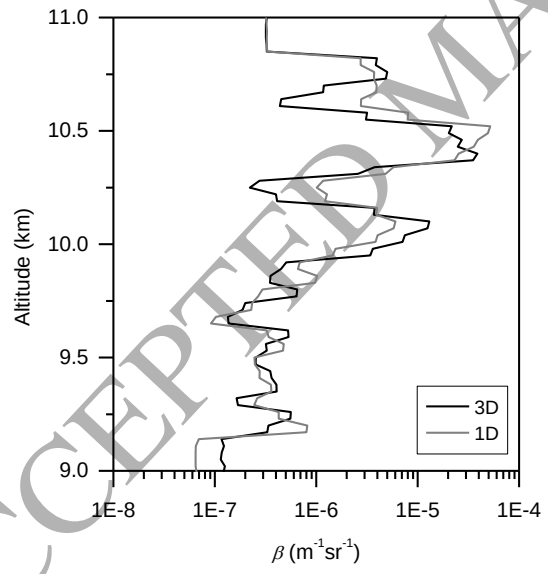

Figure 5. Profiles of the apparent attenuated backscatter: 3D case (black line) and 1D (325 m horizontal resolution) case (gray line).

3.1. Biases of the direct problem

We have to emphasize some crucial points prior to presenting our modeling results.

As was mentioned above, the random sampling was performed in this work under the following conditions: the mean profiles of the extinction coefficient $\langle\varepsilon(h)\rangle_{1D}$ and $\langle\varepsilon(h)\rangle_{3D}$ of the 1D and 3D samples are statistically equal (*i*) to one another and (*ii*) to the mean profile $\langle\varepsilon(h)\rangle_{Tot}$ of the cloud field as a whole.

In addition, our simulations were performed with a scattering matrix that was the same for all cloud pixels. Thus, $\beta(h)$ is linearly proportional to $\varepsilon(h)$ when $T^2(h) \approx 1$. Therefore, $\langle\beta(h)\rangle_{1D}$ and $\langle\beta(h)\rangle_{3D}$, as well as $\langle I(h)\rangle_{1D}$ and $\langle I(h)\rangle_{3D}$, have to be statistically equal to one another at least in the vicinity of the top of the cloud layer.

The PP bias can be understood from the following. The relationship between the apparent backscatter $\beta(h)$ and the extinction coefficient $\varepsilon(h)$ is as follows [40]:

$$\beta(h) \sim [S^{-1} \cdot \varepsilon(h) + \beta_m(h)] \cdot \exp[-2\gamma(h)\tau(h)], \tag{11}$$

where $S = \varepsilon(h)/\beta_p(h)$ is the lidar ratio (the ratio of particle extinction to backscatter); $\gamma(h)$ is a range-dependent multiple scattering function [41]. Let $\beta(h)_{i,1D}$ and $\beta(h)_{i,ICA}$ be the results of the Monte-Carlo simulations for the *i*-th observation (see Fig. 3). Under assumptions of the independent column approximation (ICA), $\beta(h)_{i,1D}$ and $\beta(h)_{i,ICA}$ can be expressed using Eq. (11) as follows:

$$\beta(h)_{i,1D} \sim \left[S^{-1} \cdot \langle\varepsilon(h)\rangle_{i,pixels} + \beta_m(h)\right] \cdot \exp\left[-2\gamma(h)\langle\tau(h)\rangle_{i,pixels}\right], \tag{12}$$

$$\beta(h)_{i,ICA} \sim \langle[S^{-1} \cdot \varepsilon(h) + \beta_m(h)] \cdot \exp[-2\gamma(h)\tau(h)]\rangle_{i,pixels}, \tag{13}$$

where $\langle\cdots\rangle_{i,pixels}$ denotes averaging over the pixels corresponding to the *i*-th observation.

Let us consider the apparent attenuated backscatter β of Eq. (11) as a nonlinear function of several independent variables. In addition, let the optical depth be proportional to the extinction coefficient, i.e., $\tau(h) = \varepsilon \cdot h$. In that case $\beta(\varepsilon, S, \beta_m, \gamma, h) \sim [\varepsilon + S \cdot \beta_m] \cdot \exp[-2\gamma \cdot \varepsilon \cdot h]$. Its second derivative with respect to ε is negative under the condition:

$$\gamma(h)[\tau(h) + S \cdot \beta_m(h) \cdot h] < 1, \tag{14}$$

that is, at small values of the optical depth.

Therefore, $\beta(h)_{i,1D}$ is greater than or equal to $\beta(h)_{i,ICA}$ according to Jensen's inequality (see, e.g, [42]). In other words, the PP bias $\Delta\beta(h)_{i,PP}$ must be positive ($\Delta\beta(h)_{i,PP} > 0$). The second derivative is positive at large values of the optical depth. Accordingly, $\Delta\beta(h)_{i,PP}$ becomes negative with increasing $\tau(h)$.

In order to understand some basic properties of the PP and ICA biases under multiple-scattering conditions, we performed simulations for the case of a very simple 3D field. A homogeneous cloud covers half of the field as viewed from the top (a two-pixels cloud field). The thickness of the cloud is 1 km and the cloud top altitude is 10 km. The extinction coefficient is 3 km^{-1}; the scattering matrix is the same as described above (see Section 2.2). The center of CALIOP laser footprint is exactly on the cloud border. In other words, a half of the laser beam passes through the cloud pixel, another half goes through the molecular-atmosphere pixel. The simulation results are shown in Fig. 6. The biases are presented in terms of the percentage with respect the true profile $\beta_{3D}(h)$ of the apparent attenuated backscatter. It is seen that the total bias is dominated by the PP bias, which corresponds to the plane-parallel cloud having the extinction coefficient 1.5 km^{-1}. At the same time, the ICA bias cannot be neglected. It reaches 27 % in our case. Another important point to underscore is the fact that all biases become negative in the molecular atmosphere below the cloud.

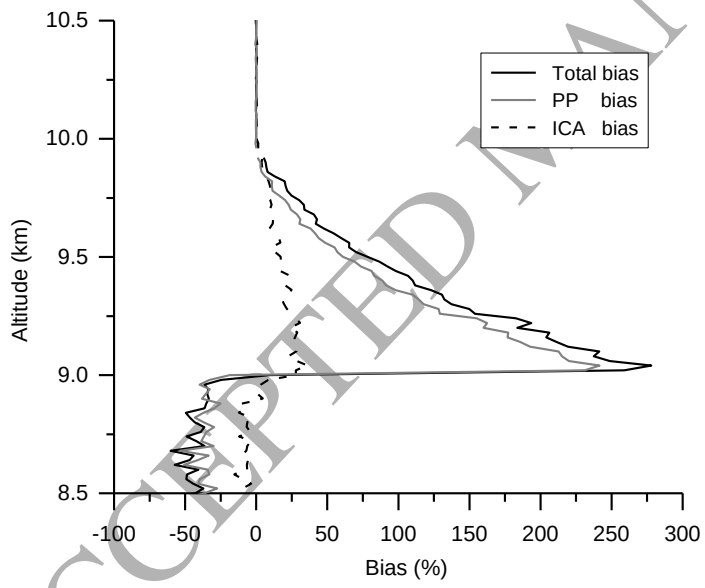

Figure 6. Total (black line), PP (gray line), and ICA (dashed line) biases of the apparent attenuated backscatter coefficient $\beta(h)$.

3.2 Effect on lidar data at 325 m and 1 km horizontal resolutions

We discuss below the effects of cirrus heterogeneity on optical properties that are directly measured by the CALIOP/CALIPSO lidar, that is, apparent attenuated backscatter, integrated apparent backscatter, and volume depolarization ratio (see, e.g., [43] p. 01). It is beyond the scope of this work to evaluate effects on derived optical characteristics, that is, those that can only be obtained via application of the CALIPSO extinction retrievals.

Effects of cirrus heterogeneity in multiple-scattering conditions are shown in Figs. 7 and 8. Note that the mean averaged biases are computed from Eqs. (3) and (4). Some resemblance between the corresponding curves of the figures comes from the fact that the data are normalized. The relative error/bias is normalized to $\langle P(h)\rangle_{3D}$ Eq. (4), and the *t*-value is normalized to the estimated variances and covariance Eq. (6). At the same time, there are differences that help to underscore some properties. The shaded rectangles in Fig. 8 correspond to the tabled critical *t*-values of $t_{.05} = \pm 1.96$. In other words, if a *t*-value of a parameter $P(h)$ is within the rectangle, we can retain the null hypothesis (see Eq. 5) meaning that there is no difference between 3D and 1D signals.

As it is expected, $\langle \beta(h)\rangle_{1D}$ and $\langle \beta(h)\rangle_{3D}$ are statistically equal at the top of the cloud layer for the both cases of the resolution (325 m and 1 km). The same is true for $\langle I(h)\rangle_{1D}$ and $\langle I(h)\rangle_{3D}$. The difference between $\langle \beta(h)\rangle_{1D}$ and $\langle \beta(h)\rangle_{3D}$ increases quickly with the penetration into the cloud layer, i.e., with decreasing altitude h, and reaches the maximum level about 20%. It follows from Fig. 6a that $\delta\beta(h)$ became significant at the altitude interval close to $h = 10.6$ km for the 325 m resolution and around $h = 10.3$ km for the 1 km resolution. The null hypothesis, that is, the hypothesis H_0: $\langle \beta(h)\rangle_{1D} = \langle \beta(h)\rangle_{3D}$, is thus rejected.

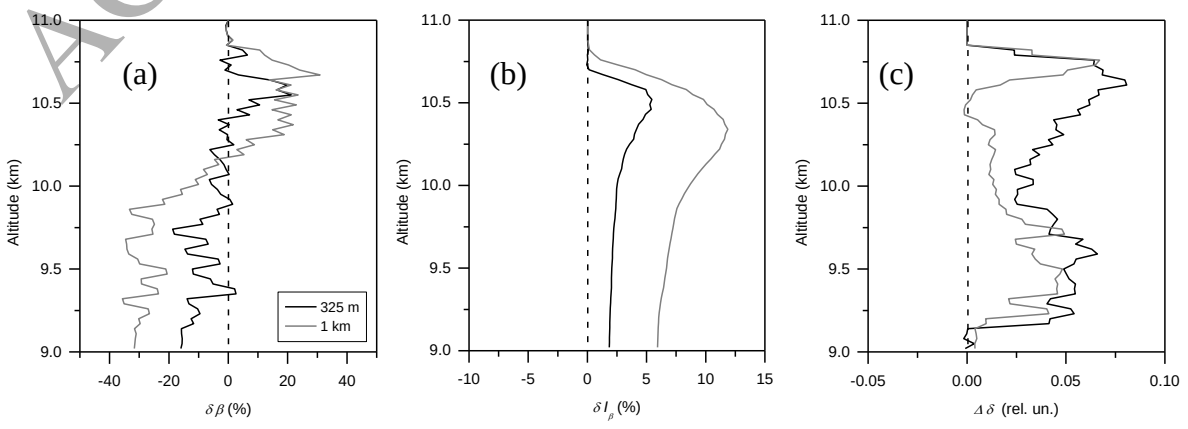

Figure 7. Deviation between 1D and 3D lidar data profiles following (Eq. 4) The black and gray lines correspond to the 325-m and 1-km horizontal resolutions, respectively. Mean relative error/bias of the apparent attenuated backscatter (a) and of the integrated apparent backscatter (b), absolute error/bias of the volume depolarization ratio (c).

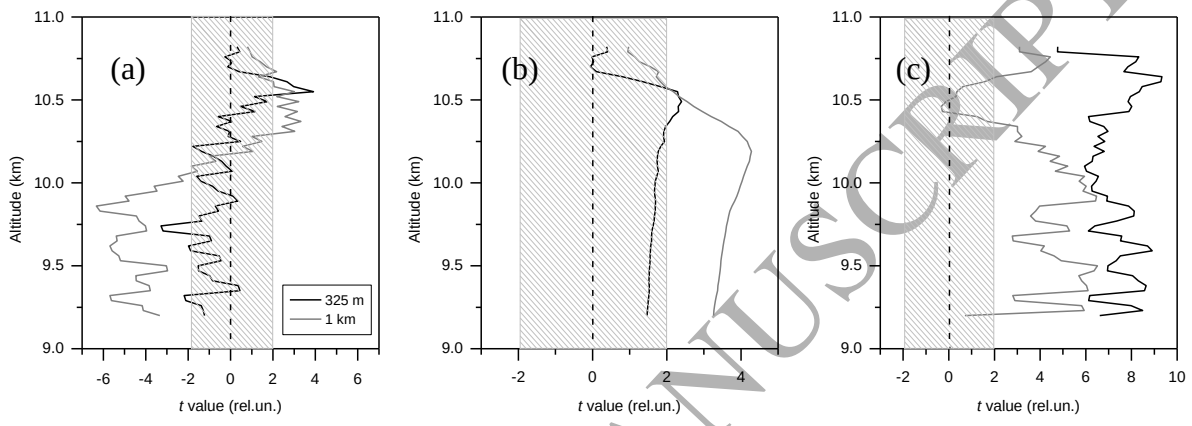

Figure 8. Profiles of the *t*-value for two dependent samples computed from Eq. 6. The black and gray lines correspond to the 325-m and 1-km horizontal resolutions, respectively. Apparent attenuated backscatter (a), integrated apparent backscatter (b), and volume depolarization ratio (c). The shaded rectangle corresponds to the critical *t*-values of $t_{.05} = \pm 1.96$.

The $\delta\beta(h)$ behavior is in agreement with the results of Section 3.1. In addition, we can hypothesize that the increasing $\delta\beta(h)$ in conditions of multiple scattering is the consequence of the horizontal photon transport (see, e.g., [44]). It was underscored in the work by Davis and Marshak [45] that the actual mean-free-path in heterogeneous optical media is always larger than that predicted by the average extinction. It means that photons have a higher probability to be scattered when they are within the field of view of the lidar receiver in the case of the 1D, i.e., horizontally homogeneous cloud. Thus, $\beta_{1D}(h)$ is higher than $\beta_{3D}(h)$ at the altitude intervals close to $h = 10.6$ and 10.3 km despite the fact that the extinction coefficients $\langle\varepsilon(h)\rangle_{1D}$ and $\langle\varepsilon(h)\rangle_{3D}$ are close to each other.

Below the maximum, the relative error $\delta\beta(h)$ decreases with increasing optical depth $\tau(h)$. That property can be explained by the following. The generated cirrus field has a multilayered structure (see the example in Fig. 5), i.e., cloud layers are alternated by layers of the molecular atmosphere. And, the total bias becomes negative in the molecular atmosphere below the cloud (see Section 3.1 and Fig. 6).

Looking at Figure 8a, we can consider $\langle\beta(h)\rangle_{1D}$ and $\langle\beta(h)\rangle_{3D}$ to be statistically equal in the case of the 325 m resolution with a few exceptions. The hypothesis H_0: $\langle\beta(h)\rangle_{1D} = \langle\beta(h)\rangle_{3D}$ is retained for almost the entire cloud layer (the black line in Fig. 8a). This is not the case for the 1 km resolution. The difference between $\langle\beta(h)\rangle_{1D}$ and $\langle\beta(h)\rangle_{3D}$ is statistically significant for a large range of the altitudes. The error $\delta\beta(h)$ reaches the values up to -30% (the gray line in Fig. 7a). The two random samplings, i.e., 325 m and 1 km horizontal resolutions, led us to opposite conclusions. Most likely statistical properties of the 3D cloud field (Fig. 1), e.g., the correlation length, caused that difference. That problem will be the subject of further research.

The behavior of the relative error/bias $\delta I(h)$ (see Fig. 7b) of the integrated apparent backscatter is in total agreement with the properties of $\delta\beta(h)$. The error $\delta I(h)$ reaches the maximal values of 4 % and 12 % for the 325 m and 1 km horizontal resolutions, respectively. The difference between $\langle I(h)\rangle_{1D}$ and $\langle I(h)\rangle_{3D}$, decreases with increasing optical depth $\tau(h)$ because $\delta\beta(h)$ becomes negative. For the 325 m resolution the hypothesis H_0: $\langle I(h)\rangle_{1D} = \langle I(h)\rangle_{3D}$ is retained for almost the entire cloud layer (the black line in Fig. 8b). In contrast the difference between $\langle I(h)\rangle_{1D}$ and $\langle I(h)\rangle_{3D}$ is statistically significant in the case of the 1 km resolution.

The absolute error/bias $\Delta\,\delta(h)$ of the volume depolarization ratio is shown in Fig. 7c. It reaches the maximal value about 0.07. On one hand, such a value is quite small compared to values of 0.33 ± 0.11 that are typical for cirrus clouds (see, e.g., [46]). On the other hand, the difference between $\langle\delta(h)\rangle_{1D}$ and $\langle\delta(h)\rangle_{3D}$ is statistically significant for the entire cloud layer (see Fig. 8c). Another important outcome of Fig. 8c is the fact that the volume depolarization ratio is always higher in the plane-parallel case, i.e., $\langle\delta(h)\rangle_{1D} \geq \langle\delta(h)\rangle_{3D}$, when the cloud consists of non-spherical ice crystals. This is a direct consequence of the fact that the depolarization ratio is much lower in the pixels without ice particles, that is, in the molecular atmosphere.

4. Conclusions

We developed two software tools for evaluating effects of 3D cloud heterogeneity on CALIOP/CALIPSO lidar data under multiple-scattering conditions. The first one is the Monte Carlo simulator (3DMcPOLID) of lidar signals. It uses a Stokes vectors representation of polarized light and takes into account particle scattering matricies, multiple scattering and the three dimensional structure of cloudy atmosphere [23]. The second tool is the high-resolution 3D cloud fields generator 3DCLOUD_V2. It provides realistic 3D cloud fields corresponding to stratocumulus, cumulus and cirrus conditions [20].

This work is devoted to evaluating the effects of cirrus heterogeneity only on optical properties that are directly measured by the lidar CALIOP/CALIPSO. That is, we analyzed effects on profiles of apparent attenuated backscatter, integrated apparent backscatter, and volume depolarization.

Our evaluations are based on random sampling. They were done by comparing mean profiles of the 3D clouds and those of the homogenous and plane-parallel equivalent 1D clouds that have the same optical characteristics as the 3D clouds on the average. The statistical significance of our results is high due to the fact that each sample consists of the large number of observations $N = 200$. We employed two complementary approaches to evaluate the plane-parallel bias, that is, the analysis of relative errors and the statistical test for difference between two related variables (paired *t*-test).

With a few exceptions, we could consider as statistically equal the profiles *(i)* of the apparent attenuated backscatter $\langle\beta(h)\rangle_{1D}$ and $\langle\beta(h)\rangle_{3D}$ as well as *(ii)* of the integrated apparent backscatter $\langle I(h)\rangle_{1D}$ and $\langle I(h)\rangle_{3D}$ when a cirrus cloud field is probed with the 325 m resolution. In contrast, the difference between $\langle\beta(h)\rangle_{1D}$ and $\langle\beta(h)\rangle_{3D}$ as well as the difference between $\langle I(h)\rangle_{1D}$ and $\langle I(h)\rangle_{3D}$ are statistically significant in the case of the 1 km resolution. As for the volume depolarization ratio profiles, they are statistically different for the both cases of the horizontal resolution.

Detailed evaluation of measurement-errors effects is beyond the scope of this article. At the same time we underscore the following. It follows from the basic principles that the variance values should be higher and the covariance values should be lower in view of measurement error. Thus, the corresponding *t*-values should decrease, see Eq. (6); and the statistical difference between profiles should become less significant. This suggests that there is only a slight bias in cirrus-cloud statistics derived from CALIOP direct data, that is, from the attenuated backscatter coefficient and/or the depolarization ratio.

The configuration of CALIOP measurements, i.e., the altitude and the receiver FOV, are such that signals from cirrus are affected by multiple scattering even at low values of the optical

depth. In addition, the total bias is dominated by the plane-parallel bias, when 3D clouds are modelled with plane-parallel equivalent 1D clouds. At the same time, the independent column approximation bias cannot be neglected.

Appendix A : 3DMcPOLID evaluation

3DMcPOLID is an enhanced version of the MC lidar simulator [47]. 3DMcPOLID is based on 3DMCPOL [18], a forward MC model using the locate estimate method to compute solutions to the vector radiative transfer equation (Stokes vectors). 3DMCPOL was developed to simulate polarized radiance at the top of the atmosphere for fully 3D cloudy atmosphere. Major modifications of 3DMCPOL were performed with the aim to adapt it to lidar tasks. Namely, 3DMcPOLID accounts for laser divergence, telescope pattern, and the time dependence of signals. Specific variance reduction techniques [48] are included for the purpose of increasing the computational efficiency. In order to evaluate 3DMcPOLID, its outputs for different atmospheric and lidar system configurations have been compared with results published in the scientific literature.

A.1. Comparison with MUSCLE community results

Comparisons between 3DMcPOLID results and those published by the MUSCLE (MUltiple Scattering in Lidar Experiments) community have been done. Detailed conditions of simulation can be found in [10, 49]. Fig. A1 shows calculated ratios of multiple-to-single scattering contributions (top row) and ratios of double-to-single scattering contributions (bottom row) to the lidar return as a function of range in uniform cloud for two values of field-of view of a receiver (10 mrad and 1 mrad). The phase function is the C1 [50] phase function at 1.064 μm. The cloud base is at 1 km and the lidar is directed vertically. The results of our simulations (grey lines) are superimposed on the published figures by Bissonnette et al. [10].

Fig. A2 shows lidar backscattered signals computed for different orders of scattering and for two values of field-of view of the receiver (10 mrad and 1 mrad) as function of range in

uniform C1 cloud. The results of our simulations (grey and black lines) are superimposed on the published figures by Winker and Poole [49]. Generally, our simulations show very good agreement with the MUSCLE results, attesting that multiple scattering processes, backscattered intensity and the field of view of laser and receiver system are well coded in 3DMcPOLID.

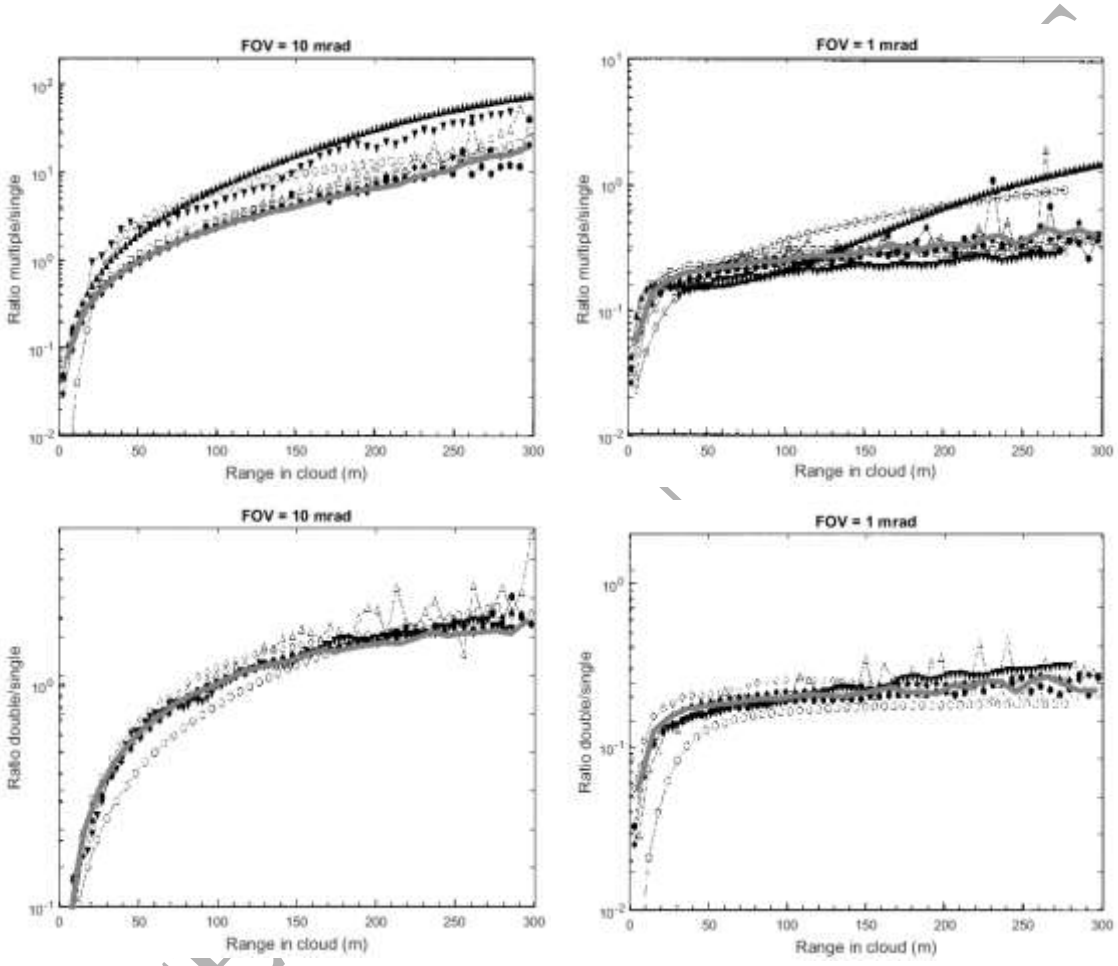

Figure A1. Calculated ratios of multiple-to-single and of double-to-single scattering contributions to the lidar return from a uniform C1 cloud for different values of receiver field of view; the cloud base is at 1 km and the lidar is directed vertically. Symbols are MUSCLE members models [10] and the grey line is 3DMcPOLID model.

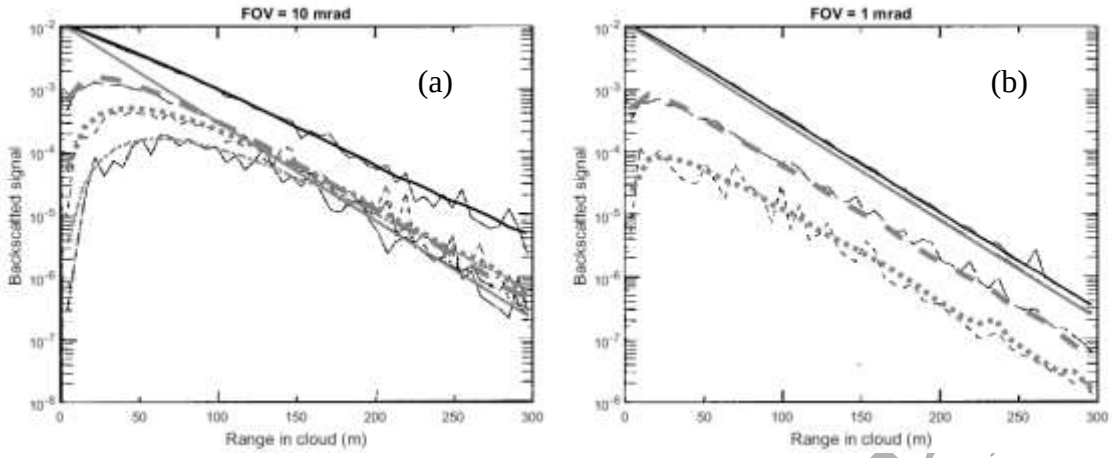

Figure A2. Solutions to the MUSCLE common problem (Winker and Poole [49]) (a) 1 mrad FOV. Curves from top to bottom are: total signal, single scatter signal, second order, third order. (b) 10 mrad FOV. Curves from top to bottom are: total signal, single scatter signal, second order, third order, fourth order. Grey and black lines are 3DMcPOLID results (black: total signal, full grey: single scatter signal, large dashed grey: second order, dotted grey: third order, small dotted grey: fourth order)

A.2. Comparison with TDTS and Monte Carlo codes

Fig.A3a shows comparisons between apparent 532-nm lidar backscatter simulated by 3DMcPOLID and by the time-dependent two-stream (TDTS) method [51] for a lidar system similar to CALIOP/CALIPSO. Concerning the atmospheric parameters, the sun is omitted, the ground albedo is assumed to be zero, molecular optical depths are modeled according to [52], the molecular phase function is computed using the Rayleigh theory and the molecular depolarization factor at 90° is equal to 0.0275. The optical depth of homogenous cloud is set to 0.3, 1.0 and 20. The cloud base and top heights are set to 9 and 10 km, respectively. The cirrus phase function is computed using the Mie theory. The effective radius of the cloud particles is 10 μm, and the size distribution is assumed to be lognormal with the effective variance of 0.02. The vertical resolution is 20 m. The lidar is at the altitude of 1000 km and is assumed to have a Gaussian transmitter with a 1/e half-angle beam divergence of 50 μrad and a receiver with a half-angle field of view (FOV) of 65 μrad. A top-hat receiver pattern is

assumed. For small ($\tau = 0.1$) and large ($\tau = 20$) cloud optical depths, the TDTS method and the 3DMcPOLID software show very good agreement. For the moderate cloud optical depth ($\tau = 3.0$), the TDTS method provides a slightly larger apparent backscatter coefficient compared to the 3DMcPOLID result.

Fig. A3b shows comparisons as Fig. A3a but for a thick cloud with no atmosphere. The results of the Monte Carlo code [53] are drawn as well. The simulation conditions correspond to the experiment 3 of I3RC, phase III, case 7 [54], that is, a semi-infinite cloud of absorbing particles with a single scattering albedo of 0.98, an extinction coefficient of 40 km^{-1}, the Henyey-Greenstein phase function with the asymmetry parameter of 0.85. Different FOV were considered; the corresponding footprint sizes are 20 m, 100 m (close to CALIOP/CALIPSO), 500 m and 5000 m. It is seen that TDTS code, the Monte Carlo code [53] and 3DMcPOLID show very similar simulated profiles of apparent backscatter coefficients. Moreover, the two Monte Carlo codes results are very close with a signal smaller than TDTS code results, whatever the FOV size, except very large FOV (footprint = 5000 m). This behavior is the same as those observed in Fig.A3a and is due to the fact that multiple scattering processes are differently treated in Monte Carlo method and in the TDTS code.

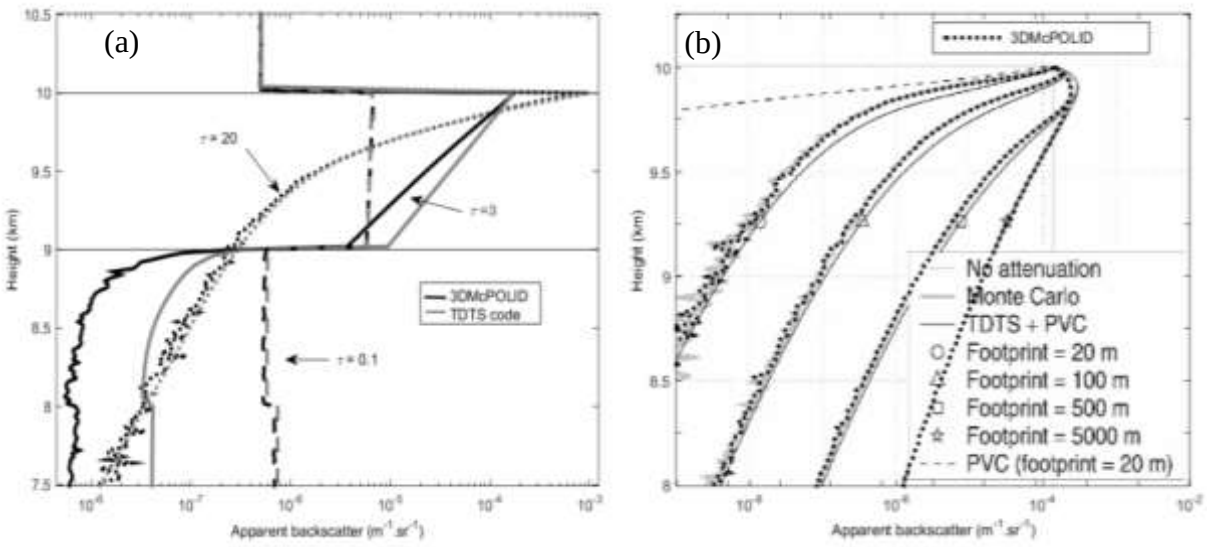

Figure A3: (a) Lidar system similar to CALIOP/CALIPSO apparent backscatter coefficient as a function of altitude for homogeneous plane parallel cirrus between 9 km and 10 km, computed with TDTS code (full line) and with 3DMcPOLID (dotted line). Three optical depths are considered, τ=0.1 (dashed line), τ=3 (full line) and τ=20 (dotted line). (b) Lidar

apparent backscatter coefficient as a function of altitude for a thick semi-infinite cloud, computed with TDTS code (black thin line), with Monte Carlo code (grey thick line) [53] and 3DMcPOLID (dotted black line), for different fields of view or footprints. Background picture of Fig.A3b is extracted from [51].

A.3. Comparison with ECSIM and an analytical model results

Fig.A4 shows profiles of linear and circular depolarization ratio for lidar sounding of a water cloud composed of spherical droplets. To be more specific, the simulations were performed for the C1 cloud and a lidar positioned at the distance of 2 km and having the receiver FOV of 1.75 mrad. The profiles are shown as a function of the cloud optical depth. The results of a Monte Carlo based code ECSIM [55], of an analytical approach [56], and of 3DMcPOLID are represented. It is seen that all tree approaches show coherent behavior of the depolarization ratio. As expected, the depolarization ratios are closed to zero at the top of the cloud. Then, the depolarization ratios gradually increase with the distance from the cloud top, i.e., with the optical depth. This increase is due to multiple scattering processes. At the same time, the depolarization ratios simulated with 3DMcPOLID are systematically a little bit larger (up to 10% for the circular depolarization) compared to data of the ECSIM code [55] and of the analytical approach [56]. For the linear depolarization ratio and for the optical depth larger than 3, the ECSIM code, the analytical approach and 3DMcPOLID provide results that are statistically identical.

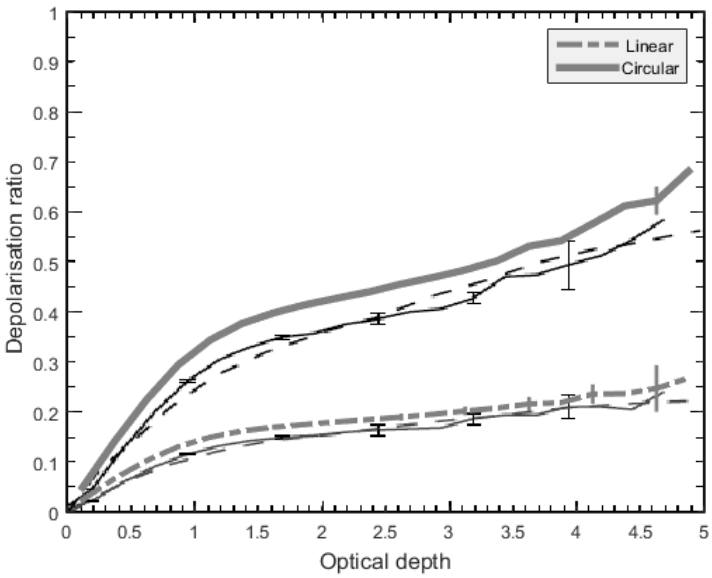

Figure A4: Linear and circular depolarization profiles in a C1 cloud at a distance of 2 km for a FOV of 1.75 mrad and a wavelength of 700 nm as a function of cloud optical depth. The grey lines show 3DMcPOLID results, solid black lines show ECSIM results [55] and dashed lines show the result calculated using an approximate analytical approach [56]. Vertical bars denote the standard deviation of the Monte-Carlo results [55]. The background figure is extracted from [55].

As the general conclusion from the evaluation results shown above we can assert that 3DMcPOLID provides fully consistent results for spaceborne and airborne lidar sounding of clouds, including polarization effects.

Acknowledgements

This work is part of the French scientific community EECLAT project (Expecting EarthCare, Learning from A-Train) and is supported by the French Centre National des Etudes Spatiales (CNES). The authors are grateful to the anonymous reviewers for their fruitful comments.

References

[1] Collins WD, Satoh M. Simulating global clouds—Past, present, and future. In: Heintzenberg J, Charlson RJ editors. Clouds in the Perturbed Climate System: Their

Relationship to Energy Balance, Atmospheric Dynamics, and Precipitation. MIT Press; 2009, p. 469–486.

[2] Boucher, O., D. Randall, P. Artaxo, C. Bretherton, G. Feingold, P. Forster, V.-M. Kerminen, Y. Kondo, H. Liao, U. Lohmann, P. Rasch, S.K. Satheesh, S. Sherwood, B. Stevens and X.Y. Zhang, 2013: Clouds and Aerosols. In: Climate Change 2013: The Physical Science Basis. Contribution of Working Group I to the Fifth Assessment Report of the Intergovernmental Panel on Climate Change [Stocker, T.F., D. Qin, G.-K. Plattner, M. Tignor, S.K. Allen, J. Boschung, A. Nauels, Y. Xia, V. Bex and P.M. Midgley (eds.)]. Cambridge University Press, Cambridge, United Kingdom and New York, NY, USA.

[3] Davis AB, Marshak A. Solar radiation transport in the cloudy atmosphere: a 3D perspective on observations and climate impacts, Rep. Prog. Phys. 2010,73: 026801. https://doi.org/10.1088/0034-4885/73/2/026801.

[4] Davies R. 3D Radiative Transfer in Satellite Remote Sensing of Cloud Properties. In: Marshak A, Davis AB, editors. 3D Radiative Transfer in Cloudy Atmospheres, Springer-Verlag, Heidelberg (Germany); 2005, p. 153-242. https://doi.org/10.1007/3-540-28519-9_11.

[5] Atlas D, Ludlam FH. Multi-wavelength radar reflectivity of hailstorms. Q. J. Roy. Meteor. Soc. 1962:88,207–208, https://doi.org/10.1002/qj.49708837626.

[6] Browning KA, Starr JR, Whyman AJ. The structure of an inversion above a convective boundary layer as observed using high-power pulsed doppler radar. Bound-Lay Meteorol. 1973:4,91–111, https://doi.org/10.1007/BF02265226.

[7] Durden SL, Haddad ZS, Kitiyakara A, Li FK. Effects of Nonuniform Beam Filling on Rainfall Retrieval for the TRMM Precipitation Radar. J. Atmos. Ocean. Tech. 1998:15,635–646. https://doi.org/10.1175/1520-0426(1998)015<0635:EONBFO>2.0.CO;2.

[8] Winker DM, Pelon J, McCormick MP. The CALIPSO mission: Spaceborne lidar for observation of aerosols and clouds. Proc. SPIE 4893, Lidar Remote Sensing for Industry and Environment Monitoring III. 2003:1–11 2003. https://doi.org/10.1117/12.466539.

[9] Winker DM, Hunt W, McGill M. Initial performance assessment of CALIOP, Geophys. Res. Lett. 2007;34:L19803. https://doi.org/10.1029/2007GL030135.

[10] Bissonnette LR, Bruscaglioni P, Ismaelli A, Zaccanti G, Cohen A, Benayahu Y, Kleiman M, Egert S, Flesia C, Schwendimann P, Starkov AV, Noormohammadian M, Oppel UG, Winker DM, Zege EP, Katsev IL, Polonsky IN. LIDAR multiple scattering from clouds. Appl. Phys. B. 1995;60:355–362. https://doi.org/10.1007/BF01082271.

[11] Bissonnette LR. Lidar and multiple scattering. In: Weitkamp C, editor. Lidar rangeresolved optical remote sensing of the atmosphere, Springer series in optical sciences, 102; 2005, ISBN 0387400753, p. 43-103.

[12] Davis AB, Marshak A, Wiscombe WJ, Cahalan RF. Scale invariance of liquid water distributions in marine stratocumulus. Part I: Spectral properties and stationarity issues. J. Atm. Sci. 1996;53:1538–1558. https://doi.org/10.1175/1520-0469(1996)053<1538:SIOLWD>2.0.CO;2.

[13] Davis AB, Marshak A, Cahalan RF, Wiscombe WJ. The Landsat scale break in stratocumulus as a three-dimensional radiative transfer effect: Implications for cloud remote sensing. J. Atmos. Sci. 1997;54:241–260. https://doi.org/10.1175/1520-0469(1997)054<0241:TLSBIS>2.0.CO;2.

[14] Davis AB, Marshak A, Gerber H, Wiscombe WJ. Horizontal structure of marine boundary layer clouds from centimeter to kilometer scales. J. Geophys. Res. 1999;104:6123–6144. https://doi.org/10.1029/1998JD200078.

[15] Cahalan RF, Ridgway W, Wiscombe WJ, Bell TL, Snider JB. The albedo of fractal stratocumulus clouds. J. Atm. Sci. 1994;51:2434–2455. https://doi.org/10.1175/1520-0469(1994)051<2434:TAOFSC>2.0.CO;2.

[16] Benassi A, Szczap F, Davis A, Masbou M, Cornet C, Bleuyard P. Thermal radiative fluxes through inhomogeneous cloud fields: a sensitivity study using a new stochastic cloud generator. Atmos. Res., Vol. 2004;72:291–315, https://doi.org/10.1016/j.atmosres.2004.03.018.

[17] Hogan RJ, Kew SF. A 3-D stochastic cloud model for investigating the radiative properties of inhomogeneous cirrus clouds. Q. J. R. Meteorol. Soc., 2005;131:2585–2608. https://doi.org/10.1256/qj.04.144.

[18] Hill PG, Hogan RJ, Manners J, Petch JC. Parametrizing the horizontal inhomogeneity of ice water content using CloudSat data products. Q. J. R. Meteorol. Soc. 2012;138:1784–1793. https://doi.org/10.1002/qj.1893.

[19] Fauchez T, Cornet C, Szczap F, Dubuisson P, Rosambert T. Impact of cirrus clouds heterogeneities on top-of-atmosphere thermal infrared radiation. Atmos. Chem. Phys. 2014;14:5599–5615. https://doi.org/10.5194/acp-14-5599-2014.

[20] Szczap F, Gour Y, Fauchez T, Cornet C, Faure T, Jourdan O, Penide G, Dubuisson P. A flexible three-dimensional stratocumulus, cumulus and cirrus cloud generator (3DCLOUD) based on drastically simplified atmospheric equations and the Fourier transform framework. Geosci. Model Develop. 2014;7:1779–1801. https://doi.org/10.5194/gmd-7-1779-2014.

[21] Miller SD, Stephens GL. Multiple scattering effects in the lidar pulse stretching problem. J. Geophys. Res., 1999;104:22,205–22,219. https://doi.org/10.1029/1999JD900481.

[22] Albers F, Reuter A, Maixner U, Levkov L, Raschke E, Sednev I. Horizontal inhomogeneities in clouds and their effect on remote particle measurements. Phys. Chem. Earth (B). 1999;24:197–202. https://doi.org/10.1016/S1464-1909(98)00037-9.

[23] Cornet C, Labonnote LC, Szczap F. Three-dimensional polarized Monte Carlo atmospheric radiative transfer model (3DMCPOL): 3D effects on polarized visible reflectances of a cirrus cloud. J. Quant. Spectrosc. Radiat. Transfer. 2010;111:174–186. https://doi.org/10.1016/j.jqsrt.2009.06.013.

[24] Gayet J-F, Ovarlez J, Shcherbakov V, Ström J, Schumann U, Minikin A, Auriol F, Petzold A, Monier M. Cirrus cloud microphysical and optical properties at southern and northern midlatitudes during the INCA experiment. J. Geophys. Res. 2004;109:D20206. https://doi.org/10.1029/ 2004JD004803.

[25] Fu Q, Carlin B, Mace G. Cirrus horizontal inhomogeneity and OLR bias. Geophys. Res. Lett. 2000;27:3341–3344. https://doi.org/10.1029/2000GL011944.

[26] Carlin B, Fu Q, Lohmann U, Mace GG, Sassen K, Comstock JM. High cloud horizontal inhomogeneity and solar albedo bias. J. Climate. 2002;15:2321–2339. https://doi.org/10.1175/1520-0442(2002)015<2321:HCHIAS>2.0.CO;2.

[27] Shonk JKP, Hogan RJ, Edwards JM, Mace GG. Effect of improving representation of horizontal and vertical cloud structure on the Earth's global radiation budget. Part I: Review and parametrization. Q.J.R. Meteorol. Soc. 2010;136:1191–1204. doi:10.1002/qj.647.

[28] Winker DM, Vaughan MA, Omar A, Hu Y, Powell KA, Liu Z, Hunt WH, Young SA. Overview of the CALIPSO mission and CALIOP data processing algorithms. J. Atmos. Ocean. Technol. 2009;26:2310–2323. https://doi.org/10.1175/2009JTECHA1281.1.

[29] Hunt WH, Winker DM, Vaughan MA, Powell KA, Lucker PL, Weimer C. Calipso lidar description and performance assessment. J. Atmos. Oceanic Technol. 2009;26:1214–1228. https://doi.org/10.1175/2009JTECHA1223.1.

[30] Nicolas F, Bissonnette LR, Flamant PH. Lidar effective multiple-scattering coefficients in cirrus clouds. Appl. Optics. 1997;36:3458–3468. https://doi.org/10.1364/AO.36.003458.

[31] Garnier A, Pelon J, Vaughan MA, Winker DM, Trepte CR, Dubuisson P. Lidar multiple scattering factors inferred from CALIPSO lidar and IIR retrievals of semi-transparent cirrus cloud optical depths over oceans. Atmos. Meas. Tech. 2015;8:2759–2774. https://doi.org/10.5194/amt-8-2759-2015.

[32] Chepfer H, Pelon J, Brogniez G, Flamant C, Trouillet V, Flamant PH. Impact of cirrus cloud ice crystal shape and size on multiple scattering effects: application to spaceborne and airborne backscatter lidar measurements during LITE mission and E LITE campaign. Geophys. Res. Lett. 1999;26:2203–2206. https://doi.org/10.1029/1999GL900474.

[33] Hogan RJ. Fast lidar and radar multiple-scattering models - 1. Small-angle scattering using the photon variance-covariance method. J. Atmos. Sci. , 2008;65:3621–3635. https://doi.org/10.1175/2008JAS2642.1.

[34] Winker DM, Pelon J, Coakley JA, Ackerman SA, Charlson RJ, Colarco PR, Flamant P, Fu Q, Hoff RM, Kittaka C, Kubar TL, Le Treut H, McCormick MP, Mégie G, Poole L, Powell K, Trepte C, Vaughan MA, Wielicki BA. The CALIPSO mission: A global 3D view of aerosols and clouds. Bull. Amer. Meteor. Soc. 2010;91:1211–1229. https://doi.org/10.1175/2010BAMS3009.1.

[35] Cho H-M et al. Frequency and causes of failed MODIS cloud property retrievals for liquid phase clouds over global oceans. J. Geophys. Res. Atmos. 2015;120:4132–4154. https://doi.org/10.1002/2015JD023161.

[36] Sheskin D. Handbook of Parametric and Nonparametric Statistical Procedures: Third Edition. 3d ed. CRC Press; 2003.

[37] Yang P, Liou KN. Geometric-optics-integral-equation method for light scattering by nonspherical ice crystals. Appl. Opt. 1996;35:6568–6584. https://doi.org/10.1364/AO.35.006568.

[38] Shcherbakov V, Gayet J-F, Jourdan O, Ström J, Minikin A. Light scattering by single ice crystals of cirrus clouds. Geophys. Res. Letters. 2006;33:L15809. https://doi.org/10.1029/2006GL026055.

[39] Davis AB, Polonsky IN. Approximation methods in atmospheric 3D radiative transfer, Part 1: Resolved variability and phenomenology. In: Marshak A, Davis AB, editors. 3D

Radiative Transfer in Cloudy Atmospheres, Springer-Verlag, Heidelberg (Germany); 2005, p. 283–340. https://doi.org/ 10.1007/3-540-28519-9_5.

[40] Winker DM. Accounting for multiple scattering in retrievals from space lidar. Proc. SPIE Int. Soc. Opt. Eng. 2003;5059:128–139. https://doi.org/10.1117/12.512352.

[41] Platt CMR. Lidar and radiometric observations of cirrus clouds, J. Atmos. Sci. 1973:30,1191–1204,. https://doi.org/ 10.1175/1520-0469(1973)030<1191:LAROOC>2.0.CO;2.

[42] Rao M, Swift R. Probability Theory with Applications, 2nd ed. Springer; 2006.

[43] CALIPSO Quality Statements: CALIPSO Quality Statements Lidar Level 2 Cloud and Aerosol Layer Products Version Releases: 3.01, 3.02. https://eosweb.larc.nasa.gov/sites/default/files/project/calipso/quality_summaries/CALIOP_L2LayerProducts_3.01.pdf; 2011 [accessed 30.01.2017].

[44] Marshak A, Davis A, Wiscombe W, Cahalan R. Radiative smoothing in fractal clouds. J. Geophys. Res. 1995;100; 26247–26261. https://doi.org/10.1029/95JD02895.

[45] Davis AB, Marshak A. Photon propagation in heterogeneous optical media with spatial correlations: Enhanced mean-free-paths and wider-thanexponential free-path distributions. J. Quant. Spectrosc. Radiat. Transfer. 2004;84:3–34. https://doi.org/10.1016/S0022-4073(03)00114-6.

[46] Sassen K, Benson S. A midlatitude cirrus cloud climatology from the facility for atmospheric remote sensing. part II: Microphysical properties derived from lidar depolarization. J. Atmos. Sci. 2001;58:2103–2112. https://doi.org/10.1175/1520-0469(2001)058<2103:AMCCCF>2.0.CO;2.

[47] Szczap F, Cornet C, Alkasem A, Gour Y, C.-Labonnote L, Jourdan O. A 3D Polarized Monte Carlo LIDAR System Simulator for Studying Effects of Cirrus Inhomogeneities on CALIOP/CALIPSO Measurements. In: Cahalan RF, editor. Radiation processes in the atmosphere and ocean (IRS2012), Proceedings. 2013, p. 139-143.

[48] Buras R, Mayer B. Efficient unbiased variance reduction techniques for Monte Carlo simulations of radiative transfer in cloudy atmospheres: The solution. J. Quant. Spectrosc. Rad. Transfer. 2011;112:434–447. https://doi.org/10.1016/j.jqsrt.2010.10.005.

[49] Winker DM, Poole LR. Monte-Carlo calculations of cloud returns for ground-based and space-based lidars. Appl. Phys. 1995;B60:341–344. https://doi.org/10.1007/BF01082269.

[50] Deimendjian D. Electromagnetic scattering on spherical polydispersions. Elsevier, New York; 1969.

[51] Hogan RJ, Battaglia A. Fast lidar and radar multiple-scattering models - 2. Wide-angle scattering using the time-dependent two-stream approximation. J. Atmos. Sci. 2008;65:3636–3651. https://doi.org/10.1175/2008JAS2643.1.

[52] Hansen JE, Travis LD. Light scattering in planetary atmospheres. Space Sci. Rev. 1974;16:527–610., https://doi.org/10.1007/BF00168069.

[53] Battaglia A, Ajewole MO, Simmer C. Evaluation of radar multiple scattering effects from a GPM perspective. Part I: model description and validation. J. Appl. Meteor. Clim. 2006;45:1634–1647. https://doi.org/10.1175/JAM2424.1.

[54] I3RC test cases, https://i3rc.gsfc.nasa.gov/cases_new.html; [accessed 03.02.2017].

[55] Donovan DP, Klein Baltink H, Henzing JS, de Roode SR, Siebesma AP. A depolarisation lidar-based method for determination of liquid-cloud microphysical properties. Atmos. Meas. Tech. 2015;8:237–266. https://doi.org/10.5194/amt-8-237-2015.

[56] Chaikovskaya L. Remote sensing of clouds using linearly and circularly polarized laser beams: techniques to compute signal polarization. In: Kokhanovsky AA editor. Light Scattering Reviews 3. Springer Praxis Books, Berlin; 2008.